J. Fluid Mech. (2017), *vol.* 824, *pp.* 388–412.
doi:10.1017/jfm.2017.356

Transitional flows with the entropic lattice Boltzmann method

B. Dorschner[1], S. S. Chikatamarla[1] and I. V. Karlin[1,†]

[1]Aerothermochemistry and Combustion Systems Laboratory, Institute of Energy Technology, Department of Mechanical and Process Engineering, ETH Zurich, 8092 Zurich, Switzerland

(Received 21 December 2016; revised 25 April 2017; accepted 19 May 2017; first published online 5 July 2017)

The accuracy and performance of entropic multi-relaxation time lattice Boltzmann models are assessed for transitional flows of engineering interest. A simulation of the flow over a low-Reynolds-number *SD*7003 airfoil at $Re = 6 \times 10^4$, at an angle of attack $\alpha = 4°$, is performed and thoroughly compared to available numerical and experimental data. In order to include blockage and curvature effects, simulations of the flow in a low-pressure turbine passage composed of *T*106 blade profiles, at a chord Reynolds number of $Re = 6 \times 10^4$ or $Re = 1.48 \times 10^5$, for different free-stream turbulence intensities are presented. Using a multi-domain grid refinement strategy in combination with Grad's boundary conditions yields good agreement for all simulations. The results demonstrate that the entropic lattice Boltzmann model is a viable, parameter-free alternative to modelling approaches such as large-eddy simulations with similar resolution requirements.

Key words: boundary layer separation, boundary layer stability, transition to turbulence

1. Introduction

Understanding of boundary layer separation, transition to turbulence and reattachment of the turbulent boundary layer is of great importance for many applications ranging from diffusers and turbine blades to micro air vehicles and unmanned air vehicles. Despite many experimental and numerical studies, improving the efficiency of engineering designs remains challenging due to the lack of predictive and controlling capabilities and requires further investigations to complement our current understanding.

Laminar separation typically occurs in the low-Reynolds-number regime, for example in the flow over an airfoil at incidence or in the flow over a flat plate with a prescribed suction profile as the upper boundary condition. On the upper surface, the boundary layer remains laminar beyond the point of minimum surface pressure and into the pressure recovery region, where the adverse pressure gradient opposes the flow and causes its detachment. Downstream of the separation point, the highly unstable separated shear layer transitions to turbulence. Subsequently, at sufficiently high Reynolds numbers or low angles of attack, the turbulent flow promotes momentum transfer in the wall-normal direction and causes reattachment of

† Email address for correspondence: karlin@lav.mavt.ethz.ch

the boundary layer, thus closing the so-called laminar separation bubble (LSB). The later the reattachment happens, the bigger the LSB and the larger the loss of lift and the increase in drag. In the limit of no reattachment and complete separation, the airfoil is said to be in a stall condition with poor aerodynamic performance. Thus, optimizing performance requires understanding and control of these mechanisms.

Recent studies were focused on the mechanism of transition to turbulence, with special attention paid to understanding the stability features of LSBs, including the role of primary and secondary instabilities in the transition process. While it was shown theoretically and experimentally by Gaster (1963) and Dovgal, Kozlov & Michalke (1994) that viscous instabilities, such as Tollmien–Schlichting (T–S) waves (see e.g. Schlichting *et al.* 1960; Ho & Huerre 1984), amplify upstream disturbances in the laminar part of the bubble, inviscid instabilities, e.g. of Kelvin–Helmholtz (K–H) type, play the dominant role in the amplification of disturbances in the free shear layer of the separation bubble and thus in the transition to turbulence (Ahuja & Burrin 1984; Watmuff 1999; Yang & Voke 2001; Lang, Rist & Wagner 2004; Yarusevych, Sullivan & Kawall 2006; Yarusevych, Kawall & Sullivan 2008; Hain, Kähler & Radespiel 2009).

One of the first direct numerical simulations (DNS) of transition over a flat plate, induced by a prescribed suction profile as the upper boundary condition, was performed by Alam & Sandham (2000). Before the transition, a staggered formation of Λ vortices was observed. Based on linear stability analysis, it was concluded that the transition process was driven by convective instability (disturbances grow in space) rather than by absolute instability (disturbances grow in time and spread everywhere). In contrast, Spalart & Strelets (2000) performed a DNS with the same set-up and observed transition of an unforced LSB with negligible T–S instabilities and no distinct regions of primary or secondary instabilities, leading to a rapid three-dimensionality.

Marxen *et al.* (2003) investigated LSBs over a flat plate by means of experiment and DNS using periodic two-dimensional disturbances upstream of the separation along with a spanwise array of spacers to trigger transition. It was observed that vortices were formed due to the roll-up of the separated shear layer, which eventually broke down to turbulence.

Subsequent investigations in Marxen, Rist & Wagner (2004) concluded that the transition was driven by convective amplification of a two-dimensional T–S wave, and that the dominant mechanism behind transition is an absolute secondary instability as proposed by Rist, Maucher & Wagner (1996), Maucher, Rist & Wagner (1997, 1999) and Rist & Maucher (2002), for which the growth of two-dimensional disturbances via viscous T–S instability upstream of the separation point undergoes a gradual transition to inviscid K–H-type amplification. The dominant downstream travelling waves quickly saturate and form large, downstream-propagating spanwise vortices. Besides this convective spatial growth, the existence of an additional temporal amplification has been observed experimentally, theoretically and numerically by Gaster (1992, 2006), Alam & Sandham (2000) and Maucher (2002), among others.

In the work of Jones, Sandberg & Sandham (2008) it was shown that although classical linear stability theory of the time-averaged flow fields suggests convective instability (Boutilier & Yarusevych 2012*a*) with no evidence of absolute instability, removing the forcing still leads to self-sustained turbulence. They concluded, based on three-dimensional simulations resolving the linear response, that transition occurs by absolute instability of two-dimensional vortex shedding within the shear layer in the absence of convectively driven transition. Further studies on flat plates and airfoils

have shown the vortex roll-up occurring in the separated shear layer at the frequency of dominant disturbance amplification with downstream vortex pairing for some flow conditions (Watmuff 1999; Lang *et al.* 2004; Burgmann, Dannemann & Schröder 2008; Zhang, Hain & Kähler 2008; Hain *et al.* 2009; Yarusevych, Sullivan & Kawall 2009). In the work by Burgmann *et al.* (2008), time-resolved measurements of the velocity field over the *SD*7003 airfoil revealed several types of coherent vortical structures developing during transition. Qualitative differences in these structures compared to the flow over flat plates, such as in Watmuff (1999) and Lang *et al.* (2004), were observed and attributed to a dependence of the transition behaviour on surface curvature as well as a dependence of the development of the coherent structures on the flow conditions. In Kurelek, Lambert & Yarusevych (2016) it was further demonstrated that the newly coalesced (due to vortex pairing) shear layer vortices, characterized by an initially high spanwise coherence, undergo rapid spanwise deformations and subsequently break down to smaller structures in the vicinity of the reattachment point.

The flow development near the reattachment point has shown significant variations depending on the surface geometry and the operating conditions. Under certain conditions, the reattachment process appears relatively steady with no shedding of large coherent spanwise vortices (Balzer & Fasel 2010), while in other cases it was observed to be an unsteady process accompanied by vortex shedding. The unsteady reattachment behaviour is called bubble flapping and was observed both experimentally and numerically, with a frequency below the one of the primary K–H instabilities (see e.g. Watmuff 1999; Boiko *et al.* 2002; Rist & Maucher 2002; Lang *et al.* 2004; Burgmann *et al.* 2008; Hain *et al.* 2009; Jones, Sandberg & Sandham 2010; Marxen & Rist 2010). To explain the cause of bubble flapping, various authors pointed at the absolute secondary instability mechanisms of the shed vortices to three-dimensional disturbances (Jones *et al.* 2008), at acoustic feedback mechanisms (Jones *et al.* 2010; Jones & Sandberg 2011) and at a viscous–inviscid coupling interacting with varying levels of free-stream turbulence (Marxen & Rist 2010). As shown by e.g. Wissink & Rodi (2004), on performing a DNS on a flat plate with different free-stream disturbances, a larger disturbance leads to a smaller bubble size, while the reattachment point is moved upstream. Similarly, Jones *et al.* (2008) observed a large decrease of the bubble size when forcing was applied, leading to a significant increase of aerodynamic performance for the NACA0012 airfoil.

Due to the lack of a comprehensive picture (Boutilier & Yarusevych 2012*b*) of the instability mechanisms at play during transition, it is inherently difficult to model these phenomena. In the work of Spalart & Strelets (2000), the accuracy of various Reynolds-averaged Navier–Stokes (RANS) turbulence models was assessed. Although the results obtained by the Spalart–Allmaras model showed reasonable agreement with the DNS, large discrepancies between the models and the reference case were observed. In particular, more sensitive quantities such as the skin friction coefficient showed significant deviations. Minor improvements of various RANS models were reported in the works of Papanicolaou & Rodi (1999), Hadzic & Hanjalic (2000) and Howard, Alam & Sandham (2000). In recent years, large-eddy simulations (LES) for transitional flows have become increasingly popular (see e.g. Wilson & Pauley 1998; Yang & Voke 2001; Roberts & Yaras 2006; Eisenbach & Friedrich 2008; Xu, Sullivan & Paraschivoiu 2010; Cadieux *et al.* 2014). While accurate results were reported for implicit LES, relying on high-order schemes for spatial derivatives to capture transition, combined with filtering for stabilization (see e.g. Galbraith & Visbal 2008; Visbal 2009; Zhou & Wang 2010), the recent work of Cadieux &

Domaradzki (2015) highlights the importance of appropriate subgrid-scale modelling by a comparison of dynamic Smagorinsky, truncated Navier–Stokes and no-model under-resolved DNS.

The motivation of the present study is to assess the recently developed entropy-based lattice Boltzmann models with respect to capturing the subtle mechanisms of transitional flows. Despite the fact that lattice Boltzmann methods (LBM) are becoming increasingly popular due to their efficiency and simplicity, stability and accuracy issues have obstructed applications to complex flows for a long time. These issues have been overcome by entropy-based LBM, which has shown encouraging results for resolved and, due to its built-in subgrid features, also coarse grid simulations (Karlin, Ferrante & Öttinger 1999; Karlin, Bösch & Chikatamarla 2014; Bösch, Chikatamarla & Karlin 2015*b*; Dorschner *et al.* 2016*a*; Dorschner, Chikatamarla & Karlin 2016*b*). In spite of validation in both laminar and turbulent flow regimes, the transition to turbulence, which not only depends on accurate prediction of the bulk flow but also is highly sensitive to the implementation of the boundary conditions, has received little attention so far in the realm of LBM. However, to establish LBM as a predictive method for engineering applications, it is of great importance to also assess the accuracy of LBM in the transitional flow regime.

The paper is organized as follows. In § 2, a brief review of entropy-based lattice Boltzmann methods is presented. Subsequently, in § 3, we consider the flow past the *SD*7003 airfoil at an angle of attack $\alpha = 4^\circ$ and a chord Reynolds number of $Re = 6 \times 10^4$. Moreover, in order to test the model's performance for highly curved geometries, simulations of the flow in a low-pressure turbine passage for different Reynolds numbers and free-stream turbulence intensities are performed and, where available, compared to DNS and experimental data. Results are discussed in § 4.

2. Entropic multi-relaxation time lattice Boltzmann models

The LBM is a promising approach to computational fluid dynamics (CFD) with applications in various regimes, such as turbulence or multiphase, thermal, compressible and micro-flows among others (Succi 2015). While conventional CFD discretizes the governing equations directly, the LBM employs discretized particle distribution functions (populations) $f_i(\boldsymbol{x}, t)$, which are designed to recover the Navier–Stokes equations in the hydrodynamic limit (Higuera & Jimenez 1989; Higuera & Succi 1989; Higuera, Succi & Benzi 1989). Each population is associated with a discrete velocity $\boldsymbol{c}_i$, $i = 1, \ldots, Q$, and these velocity vectors span a regularly spaced lattice and thus allow for a highly efficient stream–collide algorithm with exact propagation and easy parallelizability due to local nonlinearity.

In recent years, the development of LBM has made significant advances. In particular, stability issues have been overcome by the development of collision models beyond the original lattice Bhatnagar–Gross–Krook (LBGK) model. While on the one hand, the inclusion of explicit turbulence models (see e.g. Chen *et al.* 2003; Malaspinas & Sagaut 2012) has shown success, the class of parameter-free entropic lattice Boltzmann models (ELBM) has achieved accurate results for both resolved and under-resolved simulations. In particular, the notion of a discretized entropy function H was introduced in Karlin *et al.* (1999) and used to determine the relaxation of the population consistent with the second law of thermodynamics, resulting in a nonlinearly stable scheme. A key component of ELBM is the adaptive relaxation of the populations in both space and time (see e.g. Dorschner *et al.* (2016*c*) for a recent discussion on the topic in the context of multi-domain simulations).

Recently, this notion has been extended to multi-relaxation time (MRT) lattice Boltzmann models. Generally, MRT models exploit the high dimensionality of the kinetic system to choose the relaxation of higher-order, non-hydrodynamic moments in order to stabilize the scheme. For a long time, this was done by tuning the corresponding relaxation parameters (see e.g. d'Humieres 1992; Latt & Chopard 2006). In Karlin *et al.* (2014), the so-called Karlin–Bösch–Chikatamarla (KBC) model was introduced, where this issue was resolved by invoking the notion of entropy to choose the relaxation adaptively, which leads to enhanced stability and accuracy (Karlin *et al.* 2014; Bösch *et al.* 2015*b*).

The derivation of the KBC model was already discussed in Karlin *et al.* (2014), Bösch *et al.* (2015*b*) and Dorschner *et al.* (2016*a*); here we state the main steps and restrict ourselves to the isothermal case using the standard $D3Q27$ lattice.

The general lattice Boltzmann equation for the population $f_i(\boldsymbol{x}, t)$ is given by

$$f_i(\boldsymbol{x}+\boldsymbol{c}_i, t+1) = f_i' = (1-\beta) f_i(\boldsymbol{x}, t) + \beta f_i^{mirr}(\boldsymbol{x}, t), \tag{2.1}$$

where the streaming step is given by the left-hand side and the post-collision state f_i' is represented on the right-hand side by a convex linear combination of $f_i(\boldsymbol{x}, t)$ and the mirror state $f_i^{mirr}(\boldsymbol{x}, t)$.

The KBC model, as used in all simulations in this paper, represents the population f_i in terms of its natural moments as the sum of a kinematic part k_i, a shear part s_i and the remaining higher-order moments h_i:

$$f_i = k_i + s_i + h_i. \tag{2.2}$$

The mirror state is defined as

$$f_i^{mirr} = k_i + (2s_i^{eq} - s_i) + ((1-\gamma) h_i + \gamma h_i^{eq}), \tag{2.3}$$

where s_i^{eq} and h_i^{eq} denote s_i and h_i evaluated at equilibrium. The equilibrium f^{eq} is defined as the minimum of the entropy function

$$H(f) = \sum_{i=1}^{Q} f_i \ln\left(\frac{f_i}{W_i}\right), \tag{2.4}$$

subject to the local conservation laws for mass and momentum

$$\sum_{i=1}^{Q} \{1, \boldsymbol{c}_i\} f_i = \{\rho, \rho \boldsymbol{u}\}, \tag{2.5}$$

where the weights W_i are lattice-specific constants. Finally, minimizing the H function in the post-collision state yields the relaxation parameter

$$\gamma = \frac{1}{\beta} - \left(2 - \frac{1}{\beta}\right) \frac{\langle \Delta s | \Delta h \rangle}{\langle \Delta h | \Delta h \rangle}, \tag{2.6}$$

where $\Delta s_i = s_i - s_i^{eq}$ and $\Delta h_i = h_i - h_i^{eq}$ indicate the deviation from equilibrium and the entropic scalar product is given by $\langle X | Y \rangle = \sum_i (X_i Y_i / f_i^{eq})$.

The KBC model recovers the Navier–Stokes equations in the hydrodynamic limit, where the parameter β in (2.1) is related to the viscosity as

$$\nu = c_s^2 \left(\frac{1}{2\beta} - \frac{1}{2}\right), \tag{2.7}$$

where $c_s = 1/\sqrt{3}$ is the lattice speed of sound.

Finally, we mention that the transitional flows considered in this paper are sensitive to the wall boundary conditions and spurious artefacts can occur for an inappropriate choice. In the LBM framework, various propositions exist, among which only a few have been shown to be stable and accurate for both resolved and under-resolved simulations. To that end, we use the boundary condition as detailed in Dorschner *et al.* (2015, 2016*b*), which was validated for various flow set-ups including channel flow, the flow in engine-like geometries and self-propelled swimmers. Other boundary conditions used in the simulations include inflow, outflow, free-stream and periodic boundary conditions. Unless stated otherwise, we implement these boundary conditions as follows: the inflow is prescribed using equilibrium populations with unit density. For the outflow boundary, we employ the no boundary condition. The free-stream or free-slip boundary condition reflects the population with respect to the wall normal and is used to mimic an open space. The periodic boundaries are directly applied within the advection step.

3. Flow separation and transition to turbulence

In this section, we investigate two cases to test the accuracy of KBC models. In the first instance, we consider the flow over the *SD*7003 airfoil at angle of attack $\alpha = 4^\circ$ and Reynolds number $Re = 6 \times 10^4$ based on the chord length c and the inflow velocity U_∞. The second test case is regarding the flow in a low-pressure turbine passage composed of $T106A$ airfoils at Reynolds numbers of $Re = 6 \times 10^4$ and $Re = 1.48 \times 10^5$ based on the axial chord and the inflow velocity.

As stated in Cadieux & Domaradzki (2015) and also confirmed by our simulations, the key to obtaining accurate results, in agreement with experiment, is to resolve the reverse flow region near the wall and the shear layer which transitions to turbulence. Despite the efficiency of the LBM, this is an intractable task for a uniform resolution. To remedy this issue we employ the multi-domain grid refinement technique as proposed and validated for various set-ups in our recent publication (Dorschner *et al.* 2016*c*).

3.1. *Transitional flow past SD7003 airfoil*

3.1.1. *Numerical set-up*

The numerical set-up is identical to the experimental and numerical studies of Ol *et al.* (2005), Galbraith & Visbal (2008) and Zhou & Wang (2010) to allow a direct comparison with the results obtained by the KBC model.

The experimental investigations of Ol *et al.* (2005) were conducted in order to assess the suitability of three different test facilities, namely, a low turbulence wind tunnel (Technical University of Braunschweig (TU-BS) Low-Noise Wind Tunnel), a water tunnel (Air Force Research Laboratory (AFRL) Free-Surface Water Tunnel) and a tow tank (Institute for Aerospace Research (IAR) Tow Tank). While good agreement was found for IAR and TU-BS, the AFRL facility showed significantly earlier separation and reattachment, and was not able to resolve reverse flow in the bubble. The numerical study of Galbraith & Visbal (2008) was conducted to test the capabilities of implicit large-eddy simulations (ILES) to capture the LSB mechanism accurately. The use of high-order compact schemes for spatial derivatives and a Pade-type low-pass filter for stability has yielded accurate predictions of LSB for various operating points. In a similar fashion, Zhou & Wang (2010) employed an implicit LES using a high-order spectral difference method to capture the LSB.

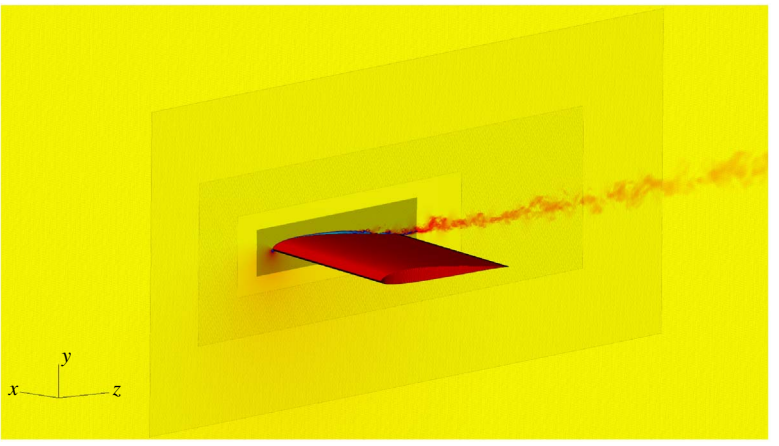

FIGURE 1. (Colour online) Multi-domain block refinement for the flow past the *SD*7003 airfoil along with a slice of instantaneous streamwise velocity.

In our study and in accordance with Galbraith & Visbal (2008) and Zhou & Wang (2010), we use a uniform inlet velocity with no inflow disturbances. A small perturbation at the beginning of the simulation is introduced to initiate vortex shedding. All statistical quantities are recorded after an initial transient of $t = 15c/U_\infty$ and collected for another $t = 45c/U_\infty$ until statistically stationary conditions have been reached. The solutions are obtained on a computational domain of $10c \times 5c \times 0.2c$ for the stream, pitch and spanwise directions, respectively. Periodic boundary conditions are applied in the spanwise direction, while free-stream boundary conditions are prescribed in the pitchwise direction. The computational domain is refined with five levels, where the coarsest level resolves the airfoil with $c = 100$ lattice points to ensure enough spatial extent to represent the reverse flow region accurately. As shown in figure 1, the refinement patches are located closely around the airfoil to minimize computational cost. Based on the maximum wall shear stress in the reattachment zone, the resolution in wall units amounts to $\Delta y^+ \approx 2.1$ at the finest level, which is similar to the ILES study of Zhou & Wang (2010) with $\Delta y^+ \approx 2.5$ using high-order spectral differences. As an additional verification of sufficient resolution, a snapshot of the spatial distribution of the stabilizer γ is shown in figure 2. It has been shown in Bösch, Chikatamarla & Karlin (2015*a*), Bösch *et al.* (2015*b*) and Dorschner *et al.* (2016*c*) that the value of γ is directly related to the degree of under-resolution and that γ automatically tends towards the LBGK value $\gamma_{lim} = 2$ in the limit of a fully resolved simulation. Therefore, the deviation of the stabilizer from its limit value indicates under-resolution. Figure 2 shows the expected small deviations from $\gamma_{lim} = 2$ at the finest grid level, suggesting negligible numerical diffusion. This assertion will be further investigated through comparison to reference data.

3.1.2. *Results*

In order to gain insight into the coherent flow structures in the LSB, we present an instantaneous snapshot of isosurfaces of the Q-criterion coloured by streamwise velocity in figure 3. As expected, starting from the leading edge, the flow remains laminar and further downstream it separates due to the adverse pressure gradient on the suction side of the airfoil. Instabilities, forming a corrugated flow pattern, and

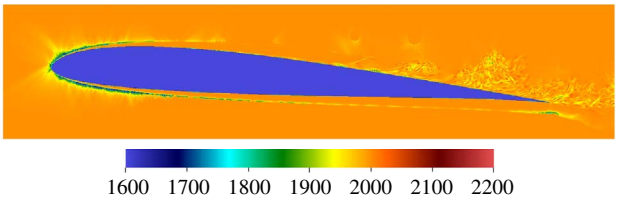

FIGURE 2. (Colour online) Instantaneous snapshot of the spatial distribution of the stabilizer γ.

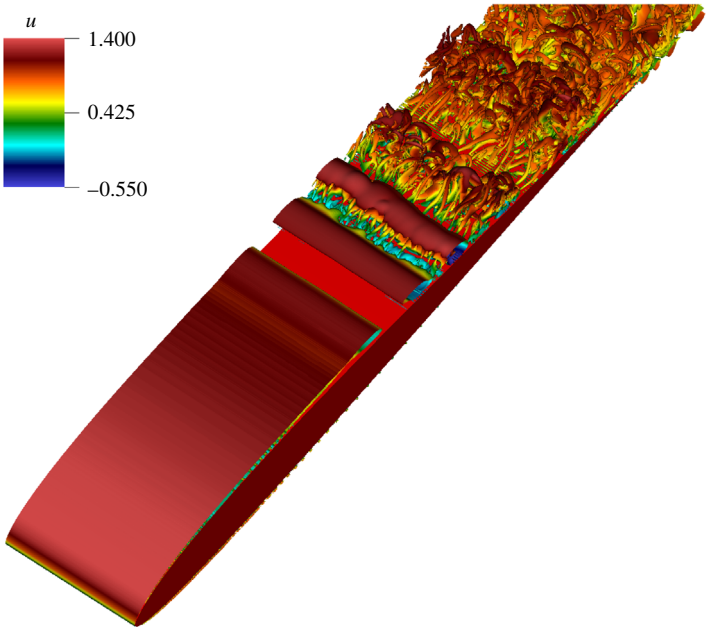

FIGURE 3. (Colour online) Isosurfaces of the Q-criterion (Q = 4) coloured by normalized streamwise velocity for the simulation of the *SD*7003 airfoil at an angle of attack $\alpha = 4°$ and a Reynolds number $Re = 6 \times 10^4$.

interaction with the small-scale structures in the recirculation zone can be observed at the end of the laminar shear layer. Further downstream, spanwise distortion leads to fully three-dimensional structures, indicating the transitional region, followed by fine-scale turbulence.

Beyond the visual inspection, one can quantify separation, transition and reattachment by computing the mean pressure coefficient $\overline{C_p} = (\overline{p} - p_\infty)/(1/2\rho_\infty u_\infty^2)$ and the mean skin friction coefficient $\overline{C_f} = \overline{\tau}/(1/2\rho_\infty u_\infty^2)$ on the airfoil surface as shown in figures 4 and 5, respectively. Here, the mean wall shear stress is denoted by $\overline{\tau}$.

The distribution of the mean pressure coefficient over the suction side of the airfoil surface can be used to extract various characteristics of the LSB. As seen in figure 4, the point of minimum pressure is followed by a pressure plateau, which has been shown to occur near the separated flow region (Tani 1964; Boutilier & Yarusevych 2012*b*). Consequently, the separation point x_s and transition location x_t can be identified as the start and the end of the pressure plateau (O'meara &

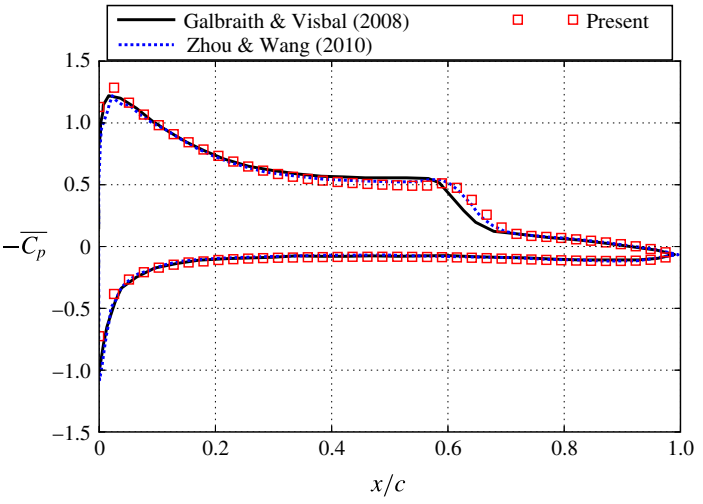

FIGURE 4. (Colour online) Average pressure coefficient $\overline{C_p}$ over the upper and lower surfaces of the *SD*7003 airfoil. Here and in the following, the symbols represent sampled values along the chord for clarity.

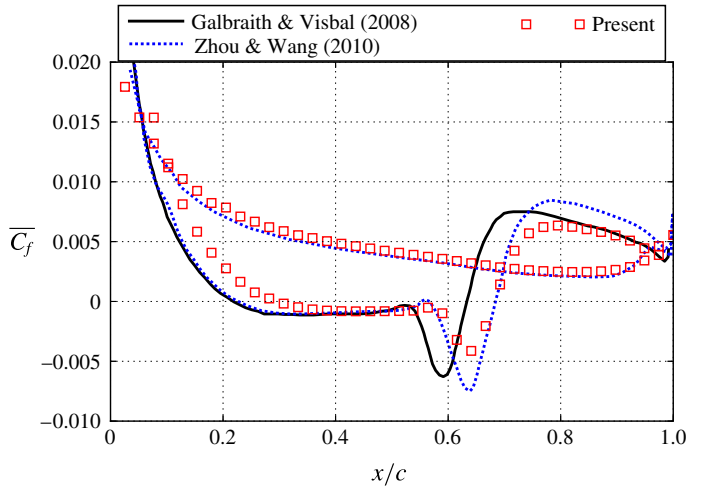

FIGURE 5. (Colour online) Average skin friction coefficient $\overline{C_f}$ over the upper and lower surfaces of the *SD*7003 airfoil.

Mueller 1987). Similarly, the reattachment point x_r can be estimated as the point at the end of the enhanced rate of pressure recovery downstream of the transition point. These definitions are commonly used to experimentally obtain LSB characteristics by linearly fitting the surface pressure data (Gerakopulos, Boutilier & Yarusevych 2010; Boutilier & Yarusevych 2012*b*). A first indication that the KBC model is able to accurately predict the mean bubble size characteristics is given by the excellent match of the $\overline{C_p}$ distribution with the high-order implicit LES of Galbraith & Visbal (2008) and Zhou & Wang (2010).

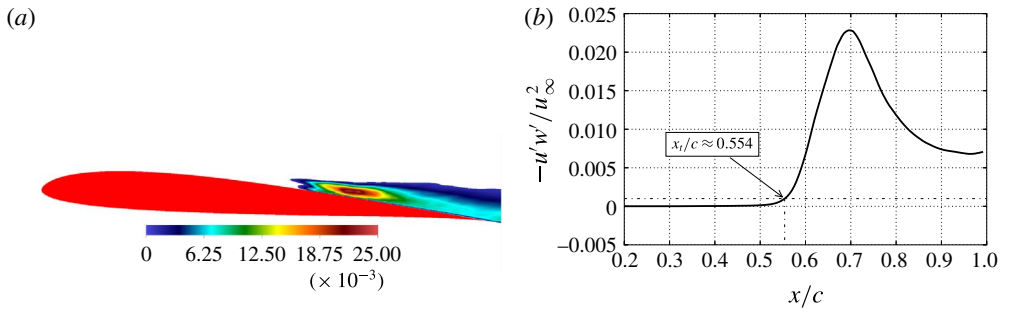

FIGURE 6. (Colour online) Determination of the onset to transition. (*a*) Distribution of Reynolds shear stress $-u'w'/u_\infty^2$ with a threshold of 0.001. (*b*) Reynolds shear stress value plotted along the line of maximum shear stress.

Contribution	*Tu* (%)	x_s/c	x_t/c	x_r/c
Ol *et al.* (2005), IAR (expt.)	0	0.33	0.57	0.63
Ol *et al.* (2005), TU-BS (expt.)	0.1	0.30	0.53	0.62
Ol *et al.* (2005), AFRL (expt.)	∼0.1	0.18	0.47	0.58
Galbraith & Visbal (2008) (ILES)	0	0.23	0.55	0.65
Zhou & Wang (2010) (ILES)	0	0.23	0.52	0.69
Present	0	0.30	0.55	0.68

TABLE 1. Comparison of the LSB properties for the flow over the *SD*7003 airfoil, where *Tu* denotes the turbulence intensity of the inflow.

On the other hand, computing the skin friction on the airfoil surface gives another meaningful way to determine the average geometrical properties of the LSB. The separation and reattachment points can be inferred from the location of zero skin friction. While the first root with a negative gradient indicates separation, reattachment happens further downstream at zero skin friction and a positive gradient. From this analysis, we report x_s and x_r along with the reference data in table 1. It is apparent that excellent agreement with the experimental data is obtained. As was mentioned above, the AFRL facility is an outlier of the experimental studies but is still reported for completeness. Furthermore, the agreement with both ILES results is reasonable. From the skin friction plot one can see that the KBC model predicts a considerably later separation as compared to the ILES but matches the experimental data. Nonetheless, the location of minimum skin friction and the reattachment location agree well with the ILES results from Zhou & Wang (2010).

Finally, in order to identify the mean location of transition, Reynolds shear stresses are considered. In figure 6(*a*), the distribution of Reynolds shear stress $-u'w'/U_\infty^2$ is shown with a threshold of 0.001. The commonly used criterion for the transition onset is the region which exceeds this threshold as these stresses describe the transport of momentum into the boundary layer (Ol *et al.* 2005; Yuan *et al.* 2005; Burgmann *et al.* 2008). Different criteria, such as the shape factor H_{12} (defined as the ratio of the displacement thickness and the momentum thickness) or the deviation from exponential growth, were identified and are in good agreement with each other (Lang *et al.* 2004; McAuliffe & Yaras 2005). In figure 6(*b*), the Reynolds shear stress value is plotted along the line of maximum shear stress, which allows us to

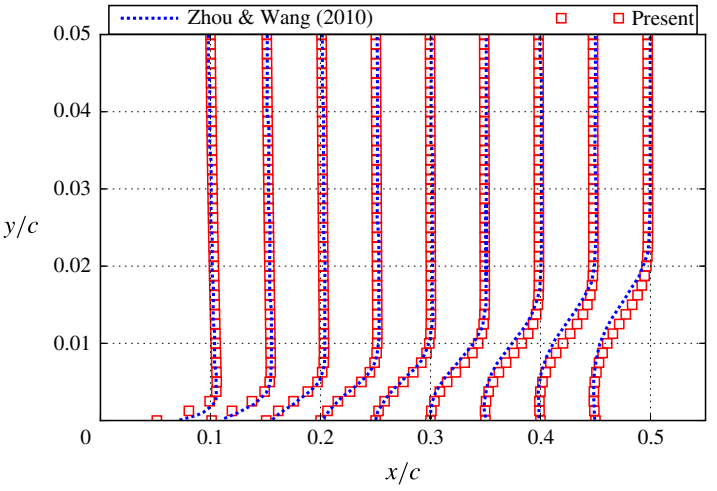

FIGURE 7. (Colour online) Mean velocity profiles at $x/c = 0.1$–0.5.

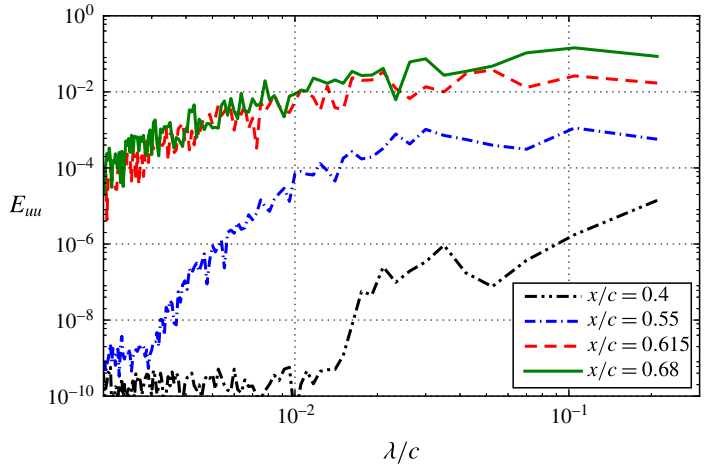

FIGURE 8. (Colour online) Spectra of fluctuating streamwise velocity along the spanwise direction.

accurately extract the transition point as the point exceeding the threshold of 0.001. The agreement with all reference data is excellent (see table 1).

The mean velocity profiles along the chord line in the wall-normal direction are compared to the ILES by Zhou & Wang (2010) in figure 7. The evolution from the attached shear layer to the detachment is clearly visible and the separation location is in line with its evaluation using the mean skin friction coefficient $\overline{C_f}$. In agreement with the previously observed deviations of the skin friction distribution over the airfoil surface, the ILES predicts earlier separation compared to both experiment and the present simulation. Nonetheless, the agreement between KBC and ILES is reasonable.

Next, we investigate the spanwise flow development. The recent experimental study of the flow over a NACA0018 airfoil by Kurelek *et al.* (2016) suggests that newly coalesced shear layer vortices possess a relatively high spanwise coherence

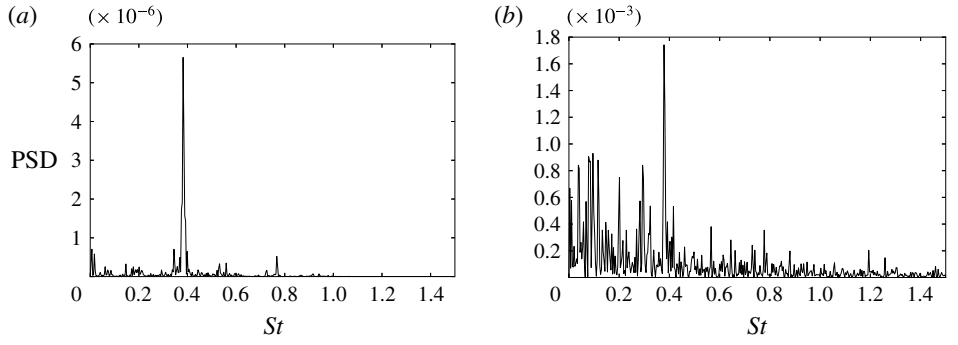

FIGURE 9. Power spectral density (PSD) for two observer points, one within the bubble and one in the near wake. (*a*) Power spectral density in the LSB at $x/c \approx 0.53$. (*b*) Power spectral density in the near wake.

and undergo a rapid spanwise deformation, which eventually leads to a break down into small-scale structures in the reattachment zone. To quantify this behaviour with the present simulation, spanwise wavelength statistics are extracted by computing the spectra of streamwise velocity fluctuations $u'u'$ along the spanwise direction for various chordwise locations within the LSB at a constant wall-normal distance of $y/c = 0.00625$. The corresponding spectra are reported in figure 8. Starting beyond the separation point at $x/c = 0.4$, one can observe that the maximum corresponds to the spanwise extent, thereby confirming the two-dimensionality of the main vortices. At the mean transition location $x/c = 0.55$, a steep increase at $\lambda/c \approx 0.01$ is followed by a plateau of dominant wavelengths ranging from $\lambda/c \approx 0.03$ to $\lambda/c \approx 0.1$. This characteristic behaviour is identical to what was observed by Kurelek *et al.* (2016) and implies three-dimensional vortex structures and weak spatial periodicity. Beyond transition onset at $x/c = 0.615$, the breakdown into small structures is evidenced by a broadening of the aforementioned plateau and an increase of the spectra at lower wavelengths. At the average reattachment point $x/c = 0.68$, the spectra practically overlap and only a minor increase at higher wavelengths is observed, suggesting a rather fast breakdown. These results agree well with the experimental study of Kurelek *et al.* (2016) and therefore confirm that the KBC model is able to capture the spanwise evolution of the flow.

Finally, the time-resolved KBC simulation allows us to study the LSB dynamics. The power spectral density of the streamwise velocity fluctuations is shown in figure 9 for two observer points, one within the LSB at $x/c \approx 0.53$ and the other in the near wake. Despite the fact that more frequencies are present in the near wake, both observer points display a dominant vortex shedding frequency at a Strouhal number $St_{vs} = f \sin(\alpha)c/U_\infty \approx 0.38$. In order to assess if the reattachment behaviour is steady or if bubble flapping occurs, the normalized bubble length l/c, which is computed through the instantaneous C_f distribution, is monitored over the course of the simulation (see figure 10*a*). A highly unsteady reattachment behaviour with various frequency contributions is evident and the bubble length fluctuates as much as $0.15l/c$ from its mean value. By employing spectral analysis and plotting the power spectral density of the bubble length (see figure 10*b*), various dominant frequencies are revealed. On the one hand, the vortex shedding frequency at St_{vs} is observed as in the analysis above. On the other hand, other dominant frequencies at lower Strouhal numbers, namely $St \approx 0.09$ and $St \approx 0.02$, are superimposed. As mentioned

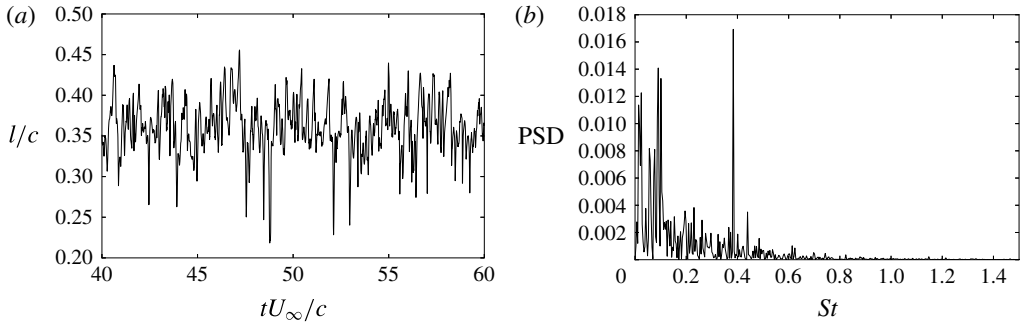

FIGURE 10. LSB dynamics. (*a*) Evolution of the bubble size. (*b*) Power spectral density for the bubble size.

in the introduction, similar behaviour was observed numerically and experimentally (see e.g. Watmuff 1999; Boiko *et al.* 2002; Rist & Maucher 2002; Lang *et al.* 2004; Burgmann *et al.* 2008; Hain *et al.* 2009; Jones *et al.* 2010; Marxen & Rist 2010). While the bubble flapping effect is confirmed by the present simulation, the cause of the low-frequency contribution is controversial in the literature and deserves further investigation in future work.

Summarizing, we have shown that the parameter-free KBC model supplied with the boundary conditions as in Dorschner *et al.* (2015, 2016*b*) is able to accurately predict the boundary layer separation, transition to turbulence and reattachment of the turbulent boundary layer. Thus, it provides a simple and efficient alternative to conventional modelling approaches such as LES. It also needs to be stressed that to accurately capture the transition phenomena it is necessary to resolve the recirculation region for which grid refinement is crucial to keep the computational cost reasonable.

3.2. *Flow in a low-pressure turbine passage*

In this section, the flow in a low-pressure turbine passage is considered. Similar to the flow past the *SD*7003 airfoil in the previous section, low-pressure turbines typically operate at relatively low Reynolds and Mach numbers. Under these conditions, depending on the geometry and the inflow, a LSB might occur. Note that, while in general compressibility effects may not be neglected for industrial applications, insight into LSB dynamics can already be gained in the incompressible flow regime (Zhang *et al.* 2015; Bigoni *et al.* 2016). The present set-up is distinctly different from the previous case of the *SD*7003 airfoil as it allows for blockage and curvature effects, as well as the unsteady wake of the blade, which can have a significant influence on the LSB and the onset of transition. In particular, the flow is redirected by more than 100° and accelerated to approximately double its inflow value, leading to a large streamwise straining where its principal axes vary spatially, as observed by Wu & Durbin (2001).

Various experimental investigations have been conducted to study LSBs in low-pressure turbines (LPTs) (Mayle 1991; Schulte & Hodson 1994; Engber & Fottner 1996; Schulte & Hodson 1998; Hodson 2000; Sieverding 2000; Hilgenfeld, Stadtmüller & Fottner 2002; Stieger & Hodson 2003). Considering the full rotor/stator arrangement in real turbine cascades, the incoming flow is highly unsteady, with wakes generated by the preceding row of blades. In the work of Schulte & Hodson (1994),

a significant effect of a periodically passing turbulent inflow wake on the LSB and thus performance was observed. Combined with hot-film measurements (Schulte & Hodson 1998), it was concluded that separation is periodically suppressed by the turbulent incoming wake and the subsequent calmed region with their full velocity profiles (see also Stieger & Hodson 2003).

On the numerical side, the increasing computing power and the relatively low Reynolds and Mach numbers in LPTs allow for DNS (see e.g. Wu *et al.* 1999; Wu & Durbin 2001). Noteworthy is the DNS study of Wu & Durbin (2001), who investigated the bypass transition due to a periodic, turbulent inflow wake, which was used to generate large free-stream disturbances.

On the modelling side, the lack of accuracy of RANS models (Raverdy *et al.* 2003) led to an increasing number of LES studies of LSBs in LPTs, focusing again on the boundary layer–wake interference (Mittal, Venkatasubramanian & Najjar 2001; Michelassi, Wissink & Rodi 2002, 2003; Rodi 2006). The results of these LES are encouraging, but uncertainties remain and high resolution is needed to capture all features of the transition. In the LES study of Michelassi *et al.* (2003) for example, significant discrepancies with the reference DNS are observed, where the LES was not capable of fully reproducing the transition location (delayed transition) and skin friction coefficient. These discrepancies are attributed to the resolution near the boundary and also in the bulk, which is not able to account for the fine-scale structures convected by the wake and thus to trigger transition.

In this paper, analogous to Raverdy *et al.* (2003), we focus on the flow past the turbine blade without an inflow wake. To analyse the effect of Reynolds number and free-stream turbulence, we conduct simulations at Reynolds numbers of $Re = 6 \times 10^4$ and $Re = 1.48 \times 10^5$ with imposed free-stream turbulence intensities in the range $Tu =$ 0–10 %.

3.3. *Numerical set-up*

The simulation set-up is identical to the DNS of Wu & Durbin (2001), who conducted incompressible flow simulations with and without a turbulent inflow wake. For comparison with experiment, the study of Engber & Fottner (1996), who carried out various experiments for different inflow disturbances and Reynolds numbers (but no turbulent wake), is considered.

The set-up consists of a single $T106$ low-pressure turbine blade, which is periodically repeated in the pitchwise direction to mimic the full turbine passage. The distance between two consecutive blade profiles is given by the normalized pitch $g/C_{ax} = 0.93$, where C_{ax} denotes the axial chord. The Reynolds number is based on the mean inflow velocity and the axial chord. The computational domain is chosen as $[-C_{ax}, 3C_{ax}] \times [-0.5g, 0.5g] \times [-0.1C_{ax}, 0.1C_{ax}]$ for the stream, pitch and spanwise directions, where the turbine blade is located at the origin. The computational cost is reduced by using three levels of grid refinement, where the coarsest level resolves the turbine blade with $C_{ax} = 300$ lattice points (see figure 11). In the case of full transition, this yields a maximum effective grid spacing of $\Delta y^+ \approx 0.25$ within the separation bubble and $\Delta y^+ \approx 2.1$ in the turbulent boundary layer at the trailing edge.

Periodic boundary conditions are applied in the pitch and spanwise directions. The exit flow has a designed angle of $-63.2°$ with the x axis and we employ convective boundary conditions at the outlet. Regarding the inflow, simulations with uniform and turbulent inflow conditions at an inlet angle of 37.7° are presented.

In order to generate the inflow turbulence, a method similar to that in Zhang *et al.* (2015) was adopted, where a frozen homogeneous isotropic turbulence field within a

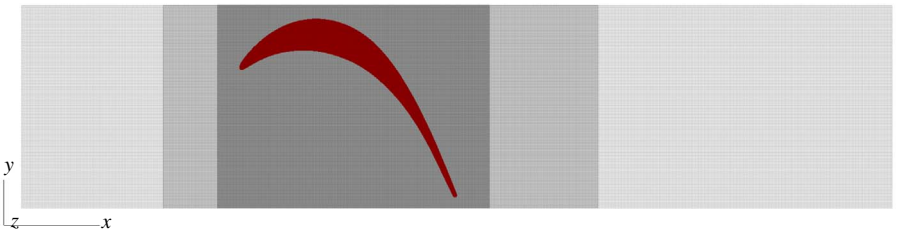

FIGURE 11. (Colour online) Computational set-up for the flow over an $T106$ turbine blade.

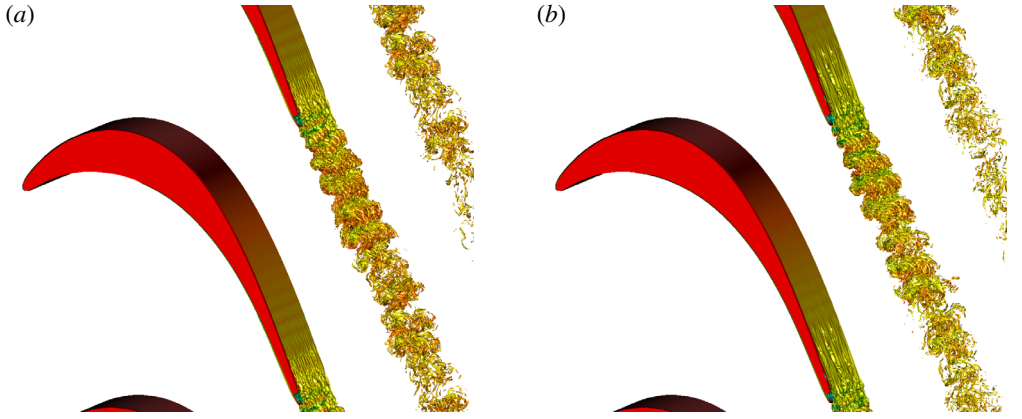

FIGURE 12. (Colour online) Flow in low-pressure turbine passage at $Re = 1.48 \times 10^5$, visualized by vorticity isosurfaces coloured by streamwise velocity. (*a*) Uniform inflow. (*b*) Turbulent inflow.

periodic box of spanwise length is superimposed onto the mean flow at the inlet angle. The box is duplicated to fill the entire inflow plane and advected with the inflow velocity to mimic time-varying fluctuations. The initial turbulence field is computed using a synthetic kinematic simulation (Fung *et al.* 1992), where the solenoidal velocity field is described as a superposition of a finite number of random Fourier modes according to an energy spectrum of the form $E(k) = Ak^4 \exp(-2k^2/k_0^2)$. The constant A and the wavenumber of the spectrum peak k_0 are chosen in accordance with the prescribed turbulence intensity.

3.4. *Results*

First, for the purpose of validation, we consider the high-Reynolds-number case of $Re = 1.48 \times 10^5$ with a uniform inflow and a turbulent inflow with $Tu = 0.2\,\%$. A snapshot of the flow in the periodically completed turbine passage is visualized in figure 12 using vorticity isosurfaces, coloured by streamwise velocity. The distribution of the pressure coefficient over both the suction and the pressure sides of the turbine blade is shown in figure 13 along with the reference data for the uniform and turbulent inflow. On the suction side, a favourable pressure gradient accelerates the flow until the adverse pressure gradient downstream of $x/C_{ax} \approx 0.6$ causes a deceleration. On the pressure side, the pressure gradient is nearly zero until $x/C_{ax} \approx 0.5$, where a steep pressure gradient accelerates the flow up to the trailing edge.

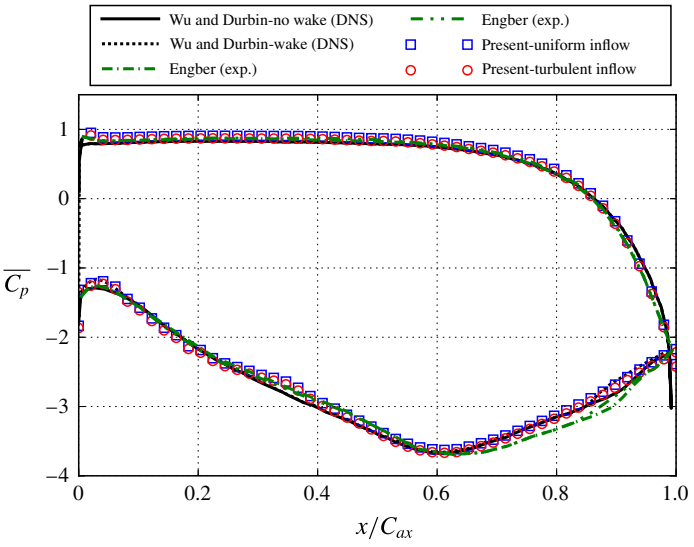

FIGURE 13. (Colour online) Distribution of the mean pressure coefficient over the axial chord of the $T106$ turbine blade at $Re = 1.48 \times 10^5$.

The comparison of the simulated pressure coefficient with the experimental and numerical data in figure 13 shows good agreement. On the pressure side, only marginal discrepancies between all data are observed. On the suction side, due to the different inflow conditions, the discrepancies are larger. The influence of the wake for the DNS data becomes apparent in the aft of the blade, where the pressure is increasing at $x/C_{ax} \approx 0.85$ compared to the uniform inlet. Similarly, minor deviations between the different inflow disturbances can be observed for the experimental data and the present simulation.

To further investigate the effect of the inflow disturbances, a close-up image zoomed in from the top in figure 14 shows the isosurfaces of the Q-criterion coloured by the normalized streamwise velocity. Both simulations exhibit Λ-type vortices at the initial stage, which subsequently develop into hairpin-type vortices. While for the simulation using a uniform inflow, these flow structures are relatively well ordered in staggered formation, the hairpin vortices for the case with a turbulent inlet are more pronounced with a higher degree of disorder.

However, as indicated by the distributions of the pressure and skin friction coefficient over the airfoil surfaces, the influence of free-stream turbulence is minor in terms of the aerodynamic quantities. In fact, the integral effects, as manifested by the drag and lift coefficients, are insignificant with deviations of less than 0.25 % and 0.01 %, respectively. While the rapid increase of the skin friction coefficient as shown in figure 15 indicates a starting transition process, full transition, as defined by the Reynolds stress criteria used above, is triggered by neither uniform nor turbulent inflow conditions. Moreover, as indicated by the skin friction coefficient and in line with DNS and LES results (Wu & Durbin 2001; Rodi 2006), the mean flow does not separate. This is in contrast to the LES by Raverdy *et al.* (2003), who reported a fully developed LSB, albeit at a lower nominal Reynolds number of $Re = 1.1 \times 10^5$ and a uniform inflow.

To investigate this discrepancy, another set of simulations was run with the same Reynolds number $Re = 1.1 \times 10^5$ as in Raverdy *et al.* (2003). However, the change in

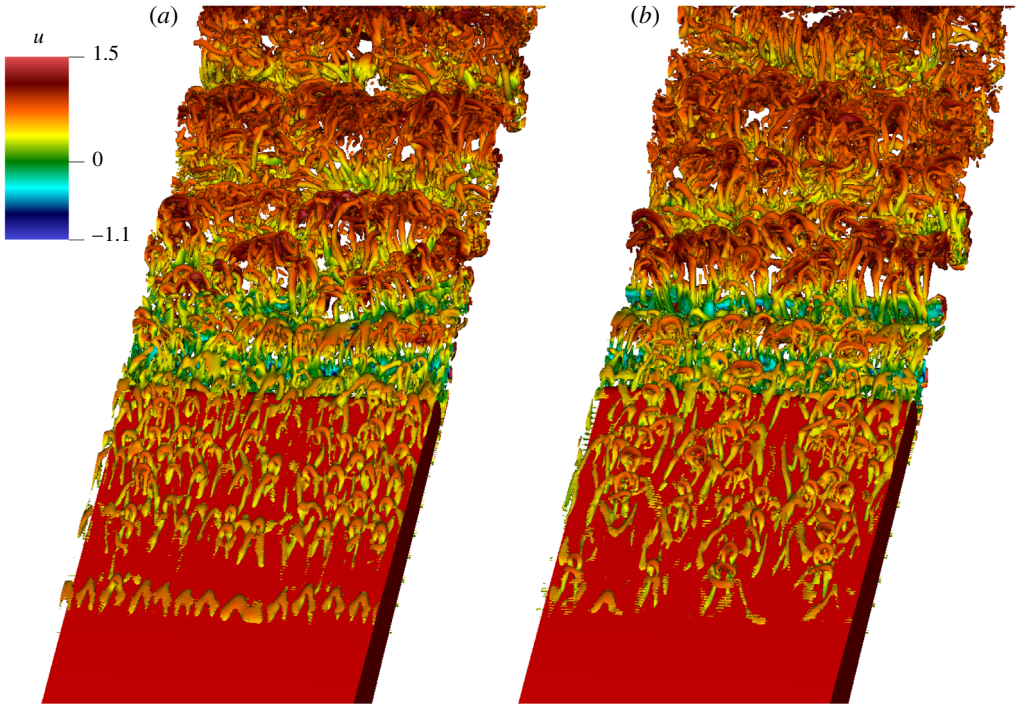

FIGURE 14. (Colour online) Snapshot of isosurfaces of the Q-criterion (Q = 200) coloured by normalized streamwise velocity at $Re = 1.48 \times 10^5$: (*a*) $Tu = 0\,\%$; (*b*) $Tu = 0.2\,\%$.

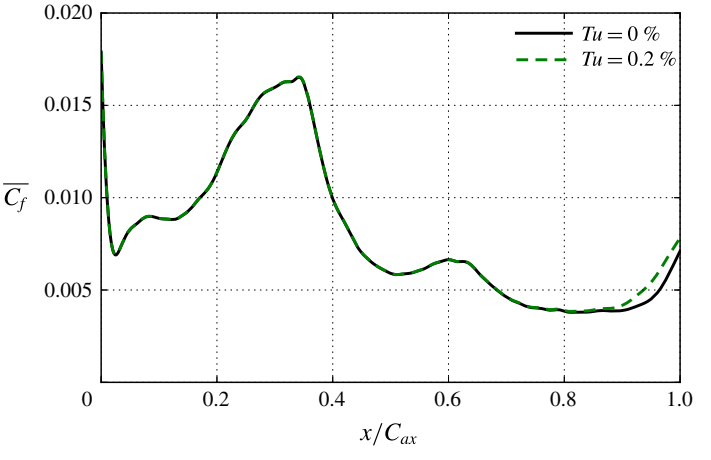

FIGURE 15. (Colour online) Distribution of the mean skin friction coefficient over the axial chord on the suction side of the *T*106 turbine blade at $Re = 1.48 \times 10^5$.

Reynolds number had only a marginal effect and no transition or mean flow separation was observed, also not under turbulent inflow conditions with $Tu = 0.2\,\%$. Thus, similar to Zhang *et al.* (2015), we decreased the Reynolds number to $Re = 6 \times 10^4$, thereby stipulating mean flow separation on the airfoil, and studied three cases with varying free-stream turbulence intensities, $Tu = \{0\,\%, 5\,\%, 10\,\%\}$. The corresponding

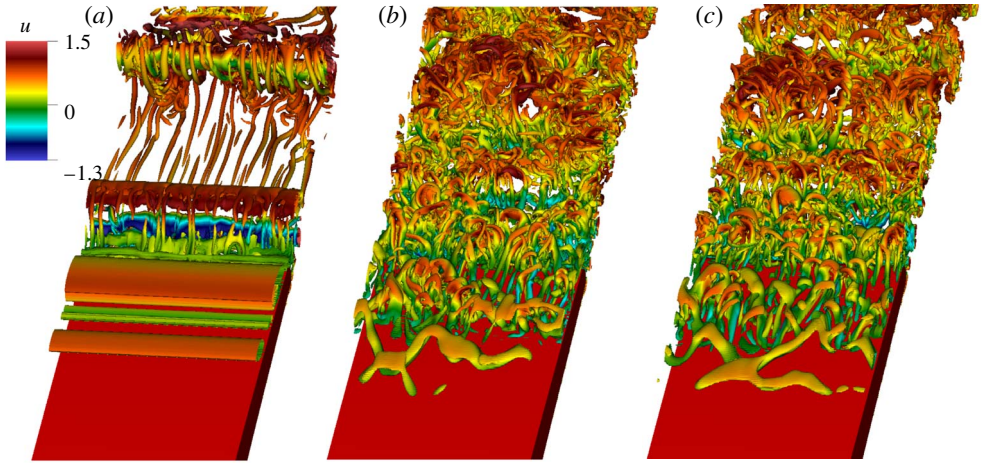

FIGURE 16. (Colour online) Snapshot of isosurfaces of the Q-criterion (Q = 110) coloured by normalized streamwise velocity at $Re = 6 \times 10^4$: (*a*) $Tu = 0\,\%$; (*b*) $Tu = 5\,\%$. (*c*) $Tu = 10\,\%$.

instantaneous snapshots showing isosurfaces of the Q-criterion, zoomed in from the top view onto the trailing edge of the blade, are shown in figure 16. It is apparent that for uniform inflow as in figure 16(*a*), the flow separates as shown by the two-dimensional vortex structures in the aft of the blade. However, turbulent structures are only developing in the wake of the blade and no natural transition occurs on the blade surface. The cases with a free-stream turbulence of $Tu = 5\,\%$ and $Tu = 10\,\%$ are shown in figure 16(*b*,*c*), respectively. It can be seen that transition is triggered for both cases, and is initiated by the formation of Λ-type vortices, similar to the high-Reynolds-number case. Further downstream these vortices develop into hairpin-type vortices, which eventually break down into fine-scale turbulence past the blade. This is in contrast to the high-Reynolds-number case, for which the boundary layer remains attached without transition to turbulence. On the other hand, in the present low-Reynolds-number cases with free-stream turbulence, separated-flow transition is observed.

The effect of free-stream turbulence on the geometrical properties of the LSB is investigated next. In figure 17 we present the skin friction coefficient for all turbulence intensities. As in Zhang *et al.* (2015), we observe that the separation location is affected by the level of free-stream turbulence and moves downstream with increasing *Tu*. In addition, the reattachment location moves upstream with increasing *Tu*, thereby reducing the extent of the entire LSB and improving aerodynamic performance. It is worth pointing out that figure 17 also shows that the effect of LSB size reduction is nonlinear with respect to *Tu*. This effect mainly stems from the nonlinear upstream shift of the reattachment location rather than the separation location, which appears to behave more linearly. Similar behaviour is shown by the mean pressure coefficient over the suction side of the airfoil in figure 18, where the pressure plateau is most pronounced for the uniform inflow case, suggesting the largest LSB. All geometrical quantities of the LSB are tabulated in table 2, where we define the onset to transition x_t as above using a threshold of $u'w'/u_\infty^2 \approx 0.001$. Investigating the flow field in more detail, we report the mean and root-mean-square (r.m.s.) streamwise velocity profiles (tangential to the blade surface on the suction side) for $x/C_{ax} = 0.88$–0.99 in steps of

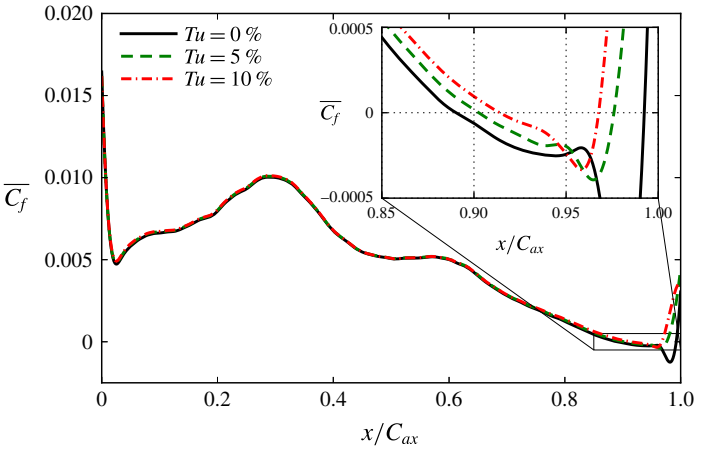

FIGURE 17. (Colour online) Average skin friction coefficient over the suction side of the $T106$ blade for varying free-stream turbulence intensities at $Re = 6 \times 10^4$.

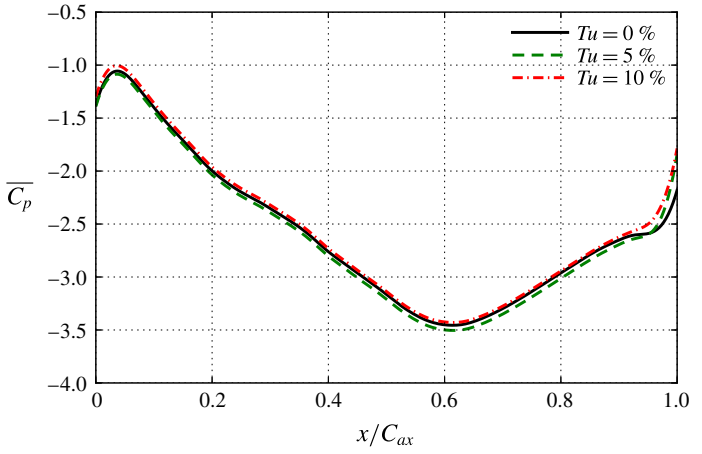

FIGURE 18. (Colour online) Average pressure coefficient over the suction side of the $T106$ blade for varying free-stream turbulence intensities at $Re = 6 \times 10^4$.

$0.1C_{ax}$ as a function of the normal distance n/C_{ax} in figure 19. The average velocity profiles in figure 19(a) confirm the visual impression from the instantaneous snapshots of a pronounced separation for the case without free-stream turbulence. For the cases including free-stream turbulence, separation is less distinct and a smaller shear layer thickness with a clear reattachment zone can be observed. Also for the mean velocity, the trend of earlier reattachment with increasing Tu is obvious. The fluctuations of the streamwise velocity component are presented in figure 19(b). In the case of uniform inflow, mild fluctuations within the separated region indicate the unsteady two-dimensional vortex rolls, whereas relatively sharp peaks of r.m.s. values are measured within the reattachment zone, which are confined to the near-wall region up to a normal distance of $n/C_{ax} \approx 0.005$. In contrast, in the case of free-stream turbulence, no vortex rolls are observed in the separation zone and the reattachment

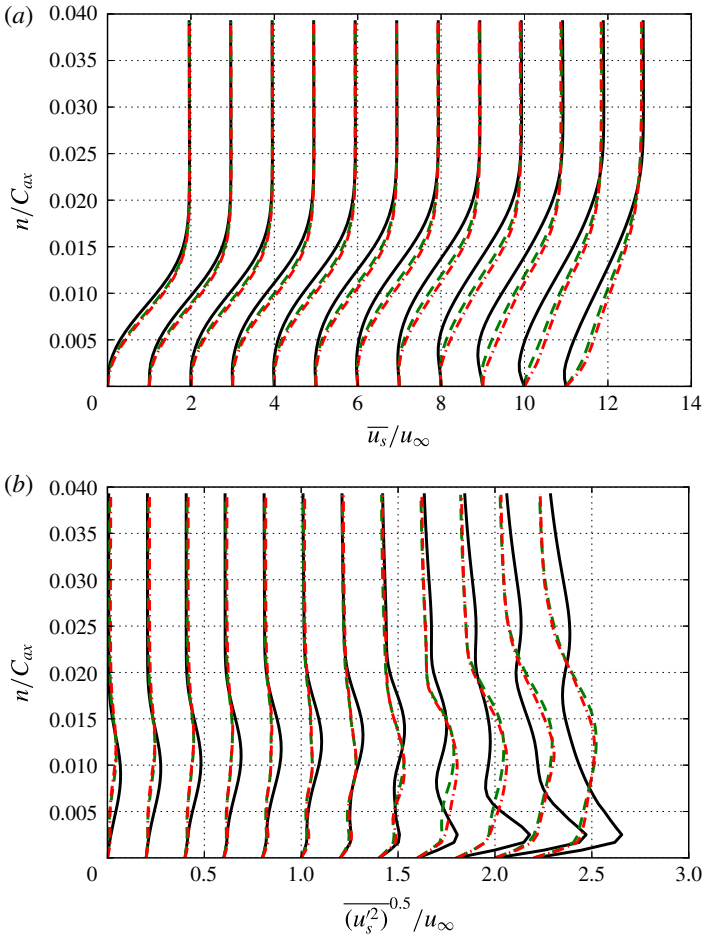

FIGURE 19. (Colour online) Streamwise velocity profiles (tangent to the suction side of the blade surface) as a function of the normal distance for $x/C_{ax} = 0.88$–0.99 in steps of $0.1C_{ax}$ at $Re = 6 \times 10^4$. (*a*) Mean streamwise velocity. (*b*) The r.m.s. streamwise velocity. For the legend see figure 18.

Tu (%)	x_s/c	x_t/c	x_r/c
0	0.890	NA	0.992
5	0.903	0.973	0.976
10	0.914	0.967	0.968

TABLE 2. Comparison of LSB properties for the flow over the $T106$ blade for different free-stream turbulence intensities at $Re = 6 \times 10^4$.

region exhibits a much broader plateau due to transition, as compared to the uniform case. This is in line with what is observed in the literature (see e.g. Raverdy *et al.* 2003).

4. Concluding remarks

Due to the lack of a comprehensive understanding of the mechanisms at play during the formation of a LSB, increasing the performance of engineering devices requires simple and efficient predictive tools. In this work, we presented a detailed investigation of entropic multi-relaxation time models and their application to transitional flows. The simulations show that the KBC model, together with Grad's boundary conditions, is capable of accurately capturing all features of LSB including separation, transition and unsteady reattachment. Although the implicit subgrid features of the KBC allow for a relatively coarse mesh resolution (Dorschner *et al.* 2016*a*), accurate results were only achieved by resolving the reverse flow region on the airfoil surface. To meet these resolution requirements, an appropriate grid refinement technique is crucial.

Thus, we have shown that the KBC model in combination with appropriate boundary conditions and grid refinement strategies is a robust, parameter-free and accurate alternative method for studying complex flows of engineering interest, where a simple grid refinement study is sufficient to ensure the validity of the simulation.

Acknowledgements

This work was supported by the European Research Council (ERC) Advanced grant no. 291094-ELBM and the ETH-32-14-2 grant. The computational resources at the Swiss National Super Computing Center CSCS were provided under the grants s492 and s630.

REFERENCES

AHUJA, K. & BURRIN, R. 1984 Control of flow separation by sound. In *9th Aeroacoustics Conference*, p. 2298. American Institute for Aeronautics and Astronautics.

ALAM, M. & SANDHAM, N. D. 2000 Direct numerical simulation of 'short' laminar separation bubbles with turbulent reattachment. *J. Fluid Mech.* **410**, 1–28.

BALZER, W. & FASEL, H. 2010 Direct numerical simulation of laminar boundary-layer separation and separation control on the suction side of an airfoil at low Reynolds number conditions. In *40th Fluid Dynamics Conference and Exhibit*, p. 4866. American Institute for Aeronautics and Astronautics.

BIGONI, F., VAGNOLI, S., ARTS, T. & VERSTRAETE, T. 2016 Detailed numerical characterization of the suction side laminar separation bubble for a high-lift low pressure turbine blade by means of RANS and LES. In *ASME Turbo Expo 2016: Turbomachinery Technical Conference and Exposition*, pp. V02DT44A015–V02DT44A015. American Society of Mechanical Engineers.

BOIKO, A. V., GREK, G. R., DOVGAL, A. V. & KOZLOV, V. V. 2002 *The Origin of Turbulence in Near-wall Flows*. Springer.

BÖSCH, F., CHIKATAMARLA, S. S. & KARLIN, I. 2015*a* Entropic multi-relaxation models for simulation of fluid turbulence. *ESAIM: Proc. Surveys* **52**, 1–24.

BÖSCH, F., CHIKATAMARLA, S. S. & KARLIN, I. V. 2015*b* Entropic multirelaxation lattice Boltzmann models for turbulent flows. *Phys. Rev.* E **92** (4), 43309.

BOUTILIER, M. S. H. & YARUSEVYCH, S. 2012*a* Separated shear layer transition over an airfoil at a low Reynolds number. *Phys. Fluids* **24** (8), 084105.

BOUTILIER, M. S. H. & YARUSEVYCH, S. 2012*b* Parametric study of separation and transition characteristics over an airfoil at low Reynolds numbers. *Exp. Fluids* **52** (6), 1491–1506.

BURGMANN, S., DANNEMANN, J. & SCHRÖDER, W. 2008 Time-resolved and volumetric PIV measurements of a transitional separation bubble on an SD7003 airfoil. *Exp. Fluids* **44** (4), 609–622.

CADIEUX, F. & DOMARADZKI, J. A. 2015 Performance of subgrid-scale models in coarse large eddy simulations of a laminar separation bubble. *Phys. Fluids* **27** (4), 045112.

CADIEUX, F., DOMARADZKI, J. A., SAYADI, T. & BOSE, S. 2014 Direct numerical simulation and large eddy simulation of laminar separation bubbles at moderate Reynolds numbers. *Trans. ASME J. Fluids Engng* **136** (6), 60902.

CHEN, H., KANDASAMY, S., ORSZAG, S., SHOCK, R., SUCCI, S. & YAKHOT, V. 2003 Extended Boltzmann kinetic equation for turbulent flows. *Science* **301** (5633), 633–636.

DORSCHNER, B., BÖSCH, F., CHIKATAMARLA, S. S., BOULOUCHOS, K. & KARLIN, I. V. 2016*a* Entropic multi-relaxation time lattice Boltzmann model for complex flows. *J. Fluid Mech.* **801**, 623–651.

DORSCHNER, B., CHIKATAMARLA, S. S., BÖSCH, F. & KARLIN, I. V. 2015 Grad's approximation for moving and stationary walls in entropic lattice Boltzmann simulations. *J. Comput. Phys.* **295**, 340–354.

DORSCHNER, B., CHIKATAMARLA, S. S. & KARLIN, I. V. 2016*b* Entropic lattice Boltzmann method for moving and deforming geometries in three dimensions. *Phys. Rev.* E (in press), arXiv:1608.04658.

DORSCHNER, B., FRAPOLLI, N., CHIKATAMARLA, S. S. & KARLIN, I. V. 2016*c* Grid refinement for entropic lattice Boltzmann models. *Phys. Rev.* E **94**, 053311.

DOVGAL, A. V., KOZLOV, V. V. & MICHALKE, A. 1994 Laminar boundary layer separation: instability and associated phenomena. *Prog. Aerosp. Sci.* **30** (1), 61–94.

EISENBACH, S. & FRIEDRICH, R. 2008 Large-eddy simulation of flow separation on an airfoil at a high angle of attack and $Re = 10^5$ using Cartesian grids. *Theor. Comput. Fluid Dyn.* **22** (3–4), 213–225.

ENGBER, M. & FOTTNER, L. 1996 The effect of incoming wakes on boundary layer transition of a highly loaded turbine cascade. *AGARD CP* **571**, 21.

FUNG, J. C. H., HUNT, J. C., MALIK, N. A. & PERKINS, R. J. 1992 Kinematic simulation of homogeneous turbulence by unsteady random Fourier modes. *J. Fluid Mech.* **236**, 281–318.

GALBRAITH, M. C. & VISBAL, M. R. 2008 Implicit large eddy simulation of low Reynolds number flow past the SD7003 airfoil. *AIAA Paper* **225**, 1–17.

GASTER, M. 1963 On the stability of parallel flows and the behaviour of separation bubbles. PhD thesis, Queen Mary, University of London.

GASTER, M. 1992 Stability of velocity profiles with reverse flow. In *Instability, Transition, and Turbulence*, pp. 212–215. Springer.

GASTER, M. 2006 Laminar separation bubbles. In *Sixth IUTAM Symposium on Laminar-Turbulent Transition*, pp. 1–13. Springer.

GERAKOPULOS, R., BOUTILIER, M. & YARUSEVYCH, S. 2010 Aerodynamic characterization of a NACA 0018 airfoil at low Reynolds numbers. In *40th Fluid dynamics conference and Exhibit*, p. 4629. American Institute of Aeronautics and Astronautics.

HADZIC, I. & HANJALIC, K. 2000 Separation-induced transition to turbulence: second-moment closure modelling. *Flow Turbul. Combust.* **63**, 153–173.

HAIN, R., KÄHLER, C. J. & RADESPIEL, R. 2009 Dynamics of laminar separation bubbles at low-Reynolds-number aerofoils. *J. Fluid Mech.* **630**, 129–153.

HIGUERA, F. J. & JIMENEZ, J. 1989 Boltzmann approach to lattice gas simulations. *Europhys. Lett.* **9** (7), 663.

HIGUERA, F. J. & SUCCI, S. 1989 Simulating the flow around a circular cylinder with a lattice Boltzmann equation. *Europhys. Lett.* **8** (6), 517.

HIGUERA, F. J., SUCCI, S. & BENZI, R. 1989 Lattice gas dynamics with enhanced collisions. *Europhys. Lett.* **9** (4), 345.

HILGENFELD, L., STADTMÜLLER, P. & FOTTNER, L. 2002 Experimental investigation of turbulence influence of wake passing on the boundary layer development of highly loaded turbine cascade blades. *Flow Turbul. Combust.* **69** (3–4), 229–247.

HO, C.-M. & HUERRE, P. 1984 Perturbed free shear layers. *Annu. Rev. Fluid Mech.* **16** (1), 365–422.

HODSON, H. 2000 Turbulence modelling for unsteady flows in axial turbine: turmunsflat. In *Brite-Euram Project, Final Tech. Rep.* CT96-1043, von Karman Institute, pp. 85–99.

HOWARD, R. J. A., ALAM, M. & SANDHAM, N. D. 2000 Two-equation turbulence modelling of a transitional separation bubble. *Flow Turbul. Combust.* **63** (1), 175–191.

D'HUMIERES, D. 1992 Rarefied gas dynamics: theory and simulations. *Prog. Aeronaut. Astronaut.* **159**, 450–458.

JONES, L. E. & SANDBERG, R. D. 2011 Numerical analysis of tonal airfoil self-noise and acoustic feedback-loops. *J. Sound Vib.* **330** (25), 6137–6152.

JONES, L. E., SANDBERG, R. D. & SANDHAM, N. D. 2008 Direct numerical simulations of forced and unforced separation bubbles on an airfoil at incidence. *J. Fluid Mech.* **602**, 175–207.

JONES, L. E., SANDBERG, R. D. & SANDHAM, N. D. 2010 Stability and receptivity characteristics of a laminar separation bubble on an aerofoil. *J. Fluid Mech.* **48** (2), 414–426.

KARLIN, I. V., BÖSCH, F. & CHIKATAMARLA, S. S. 2014 Gibbs' principle for the lattice-kinetic theory of fluid dynamics. *Phys. Rev.* E **90** (3), 31302.

KARLIN, I. V., FERRANTE, A. & ÖTTINGER, H. C. 1999 Perfect entropy functions of the lattice Boltzmann method. *Europhys. Lett.* **47** (2), 182–188.

KURELEK, J. W., LAMBERT, A. R. & YARUSEVYCH, S. 2016 Coherent structures in the transition process of a laminar separation bubble. *AIAA J.* **54** (8), 1–15.

LANG, M., RIST, U. & WAGNER, S. 2004 Investigations on controlled transition development in a laminar separation bubble by means of LDA and PIV. *Exp. Fluids* **36** (1), 43–52.

LATT, J. & CHOPARD, B. 2006 Lattice Boltzmann method with regularized pre-collision distribution functions. *Maths Comput. Simul.* **72** (2–6), 165–168.

MALASPINAS, O. & SAGAUT, P. 2012 Consistent subgrid scale modelling for lattice Boltzmann methods. *J. Fluid Mech.* **700**, 514–542.

MARXEN, O., LANG, M., RIST, U. & WAGNER, S. 2003 A combined experimental/numerical study of unsteady phenomena in a laminar separation bubble. *Flow Turbul. Combust.* **71** (1), 133–146.

MARXEN, O. & RIST, U. 2010 Mean flow deformation in a laminar separation bubble: separation and stability characteristics. *J. Fluid Mech.* **660**, 37–54.

MARXEN, O., RIST, U. & WAGNER, S. 2004 Effect of spanwise-modulated disturbances on transition in a separated boundary layer. *AIAA J.* **42** (5), 937–944.

MAUCHER, U. 2002 Numerical investigations on the transition in the laminar separation bubble in an airfoil boundary layer. PhD thesis, University of Stuttgart.

MAUCHER, U., RIST, U. & WAGNER, S. 1997 Secondary instabilities in a laminar separation bubble. In *New results in Numerical and Experimental Fluid Mechanics*, pp. 229–236. Vieweg+Teubner.

MAUCHER, U., RIST, U. & WAGNER, S. 1999 Transitional structures in a laminar separation bubble. In *New Results in Numerical and Experimental Fluid Mechanics II*, pp. 307–314. Springer.

MAYLE, R. E. 1991 The 1991 IGTI scholar lecture: the role of laminar-turbulent transition in gas turbine engines. *Trans. ASME J. Turbomach.* **113** (4), 509–536.

MCAULIFFE, B. R. & YARAS, M. I. 2005 Separation-bubble-transition measurements on a low-Re airfoil using particle image velocimetry. In *ASME Turbo Expo 2005: Power for Land, Sea, and Air*, pp. 1029–1038. American Society of Mechanical Engineers.

MICHELASSI, V., WISSINK, J. G. & RODI, W. 2003 Large-eddy simulation of flow around low-pressure turbine blade with incoming wakes. *AIAA J.* **41** (11), 2143–2156.

MICHELASSI, V., WISSINK, J. & RODI, W. 2002 Analysis of DNS and LES of flow in a low pressure turbine cascade with incoming wakes and comparison with experiments. *Flow Turbul. Combust.* **69** (3–4), 295–330.

MITTAL, R., VENKATASUBRAMANIAN, S. & NAJJAR, F. M. 2001 Large-eddy simulation of flow through a low-pressure turbine cascade. *Mech. Engng* 1–9.

OL, M., MCCAULIFFE, B., HANFF, E., SCHOLZ, U. & KAEHLER, C. 2005 Comparison of laminar separation bubble measurements on a low Reynolds number airfoil in three facilities. In *35th AIAA Fluid Dynamics Conference and Exhibit*, p. 5149. American Institute for Aeronautics and Astronautics.

O'MEARA, M. & MUELLER, T. 1987 Laminar separation bubble characteristics on an airfoil at low Reynolds numbers. *AIAA J.* **25** (8), 1033–1041.

PAPANICOLAOU, E. L. & RODI, W. 1999 Computation of separated-flow transition using a two-layer model of turbulence. *Trans. ASME J. Turbomach.* **121** (January 1999), 78–87.

RAVERDY, B., MARY, I., SAGAUT, P. & LIAMIS, N. 2003 High-resolution large-eddy simulation of flow around low-pressure turbine blade. *AIAA J.* **41** (3), 390–397.

RIST, U. & MAUCHER, U. 2002 Investigations of time-growing instabilities in laminar separation bubbles. *Eur. J. Mech. (*B*/Fluids)* **21** (5), 495–509.

RIST, U., MAUCHER, U. & WAGNER, S. 1996 Direct numerical simulation of some fundamental problems related to transition in laminar separation bubbles. In *Proceedings of the ECCOMAS Computational Fluid Dynamics Conference*, pp. 319–325. Wiley.

ROBERTS, S. K. & YARAS, M. I. 2006 Large-eddy simulation of transition in a separation bubble. *Trans. ASME J. Fluids Engng* **128** (2), 232.

RODI, W. 2006 DNS and LES of some engineering flows. *Fluid Dyn. Res.* **38** (2–3), 145–173.

SCHLICHTING, H., GERSTEN, K., KRAUSE, E., OERTEL, H. & MAYES, K. 1960 *Boundary-Layer Theory*. vol. 7. Springer.

SCHULTE, V. & HODSON, H. 1994 Wake-separation bubble interaction in low pressure turbines. In *30th Joint Propulsion Conference and Exhibit*, American Institute of Aeronautics and Astronautics.

SCHULTE, V. & HODSON, H. P. 1998 Unsteady wake-induced boundary layer transition in high lift LP turbines. *Trans. ASME J. Turbomach.* **120** (1), 28.

SIEVERDING, C. 2000 Simulation of a wake-blade interaction. *Tech. Rep.*, Brite EURAM Project TURMUNSFLAT, CT96-0143, 2000, Final Report.

SPALART, P. R. & STRELETS, M. K. 2000 Mechanisms of transition and heat transfer in a separation bubble. *J. Fluid Mech.* **403**, 329–349.

STIEGER, R. D. & HODSON, H. P. 2003 The transition mechanism of highly-loaded LP turbine blades. *ASME Conf. Proc.* **2003** (36886), 779–788.

SUCCI, S. 2015 Lattice Boltzmann 2038. *Europhys. Lett.* **109** (5), 50001.

TANI, I. 1964 Low-speed flows involving bubble separations. *Prog. Aerosp. Sci.* **5**, 70–103.

VISBAL, M. R. 2009 High-fidelity simulation of transitional flows past a plunging airfoil. *AIAA J.* **47** (January), 2685–2697.

WATMUFF, J. H. 1999 Evolution of a wave packet into vortex loops in a laminar separation bubble. *J. Fluid Mech.* **397**, 119–169.

WILSON, P. G. & PAULEY, L. L. 1998 Two- and three-dimensional large-eddy simulations of a transitional separation bubble. *Phys. Fluids* **10** (11), 2932.

WISSINK, J. & RODI, W. 2004 DNS of a laminar separation bubble affected by free-stream disturbances. In *Direct and Large-Eddy Simulation V*, pp. 213–220. Springer.

WU, X. & DURBIN, P. A. 2001 Evidence of longitudinal vortices evolved from distorted wakes in a turbine passage. *J. Fluid Mech.* **446**, 199–228.

WU, X., JACOBS, R. G., HUNT, J. C. & DURBIN, P. A. 1999 Simulation of boundary layer transition induced by periodically passing wakes. *J. Fluid Mech.* **398**, 109–153.

XU, T., SULLIVAN, P. & PARASCHIVOIU, M. 2010 Fast large-eddy simulation of low Reynolds number flows over a NACA0025. *J. Aircraft* **47** (1), 328–333.

YANG, Z. & VOKE, P. R. 2001 Large-eddy simulation of boundary-layer separation and transition at a change of surface curvature. *J. Fluid Mech.* **439**, 305–333.

YARUSEVYCH, S., KAWALL, J. G. & SULLIVAN, P. E. 2008 Separated-shear-layer development on an airfoil at low Reynolds numbers. *AIAA J.* **46** (12), 3060–3069.

YARUSEVYCH, S., SULLIVAN, P. E. & KAWALL, J. G. 2006 Coherent structures in an airfoil boundary layer and wake at low Reynolds numbers. *Phys. Fluids* **18** (4).

YARUSEVYCH, S., SULLIVAN, P. E. & KAWALL, J. G. 2009 On vortex shedding from an airfoil in low-Reynolds-number flows. *J. Fluid Mech.* **632**, 245–271.

YUAN, W., KHALID, M., WINDTE, J., SCHOLZ, U. & RADESPIEL, R. 2005 An investigation of low-Reynolds-number flows past airfoils. In *23rd AIAA Applied Aerodynamics Conference (July 2015)*, pp. 1–19. American Institute for Aeronautics and Astronautics.

ZHANG, W., HAIN, R. & KÄHLER, C. J. 2008 Scanning PIV investigation of the laminar separation bubble on a SD7003 airfoil. *Exp. Fluids* **45** (4), 725–743.

ZHANG, W., ZOU, Z., QI, L., YE, J. & WANG, L. 2015 Effects of freestream turbulence on separated boundary layer in a low-Re high-lift LP turbine blade. *Comput. Fluids* **109**, 1–12.

ZHOU, Y. & WANG, Z. J. 2010 Implicit large eddy simulation of transitional flow over a SD7003 wing using high-order spectral difference method. In *40th Fluid Dynamics Conference and Exhibit*, p. 2010. American Institute for Aeronautics and Astronautics.